JACS
JOURNAL OF THE AMERICAN CHEMICAL SOCIETY
Article
Cite This: J. Am. Chem. Soc. 2018, 140, 8696−8704
pubs.acs.org/JACS

1T′ Transition Metal Telluride Atomic Layers for Plasmon-Free SERS at Femtomolar Levels

Li Tao,[†,○] Kun Chen,[*,‡,○] Zefeng Chen,[†,○] Chunxiao Cong,[§] Caiyu Qiu,[∥] Jiajie Chen,[⊥] Ximiao Wang,[‡] Huanjun Chen,[‡] Ting Yu,[#] Weiguang Xie,[▽] Shaozhi Deng,[‡] and Jian-Bin Xu[*,†]

[†]Department of Electronic Engineering, The Chinese University of Hong Kong, Shatin, N.T., Hong Kong SAR, China
[‡]State Key Laboratory of Optoelectronic Materials and Technologies, School of Electronics and Information Technology and Guangdong Province Key Laboratory of Display Material, Sun Yat-sen University, Guangzhou 510275, China
[§]State Key Laboratory of ASIC and System, School of Information Science and Technology, Fudan University, Shanghai 200433, China
[∥]College of Microelectronics, Department of Information Science & Electronic Engineering, Zhejiang University, Hangzhou 310027, China
[⊥]Department of Biomedical Engineering, The Chinese University of Hong Kong, Shatin, N.T., Hong Kong SAR, China
[#]School of Physical and Mathematical Sciences, Nanyang Technological University, Singapore 637371, Singapore
[▽]Siyuan Laboratory, Guangdong Provincial Engineering Technology Research Center of Vacuum Coating Technologies and New Energy Materials, Department of Physics, Jinan University, Guangzhou 510632, China

Supporting Information

ABSTRACT: Plasmon-free surface enhanced Raman scattering (SERS) based on the chemical mechanism (CM) is drawing great attention due to its capability for controllable molecular detection. However, in comparison to the conventional noble-metal-based SERS technique driven by plasmonic electromagnetic mechanism (EM), the low sensitivity in the CM-based SERS is the dominant barrier toward its practical applications. Herein, we demonstrate the 1T′ transition metal telluride atomic layers (WTe_2 and $MoTe_2$) as ultrasensitive platforms for CM-based SERS. The SERS sensitivities of analyte dyes on 1T′-W(Mo)Te_2 reach EM-comparable ones and become even greater when it is integrated with a Bragg reflector. In addition, the dye fluorescence signals are efficiently quenched, making the SERS spectra more distinguishable. As a proof of concept, the SERS signals of analyte Rhodamine 6G (R6G) are detectable even with an ultralow concentration of 40 (400) fM on pristine 1T′-W(Mo)Te_2, and the corresponding Raman enhancement factor (EF) reaches 1.8×10^9 (1.6×10^8). The limit concentration of detection and the EF of R6G can be further enhanced into 4 (40) fM and 4.4×10^{10} (6.2×10^9), respectively, when 1T′-W(Mo)Te_2 is integrated on the Bragg reflector. The strong interaction between the analyte and 1T′-W(Mo)Te_2 and the abundant density of states near the Fermi level of the semimetal 1T′-W(Mo)Te_2 in combination gives rise to the promising SERS effects by promoting the charge transfer resonance in the analyte-telluride complex.

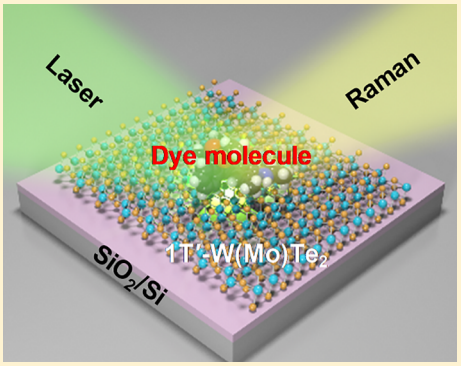

INTRODUCTION

The weak Raman signals of a molecule can be dramatically boosted by the surface-enhanced Raman scattering (SERS), making this technique capable of label-free detection at trace or even single-molecule levels.[1,2] As a nondestructive approach, SERS has stepped into various analytical applications including environmental detection, biological/medical sensing, molecular fingerprint identification, and catalysis chemistry.[1,3] The conventional SERS materials are based on noble metals with roughened surface morphologies, in which the Raman intensity can be enhanced by a factor of 10^6 or higher.[4,5] The surface plasmon resonance (SPR) induced local field magnification (mostly lies in the "hot spots": the gaps between nanostructured metal particles), regarded as the electromagnetic mechanism (EM), serves as the dominant contribution to the Raman enhancement.[4] However, the EM-based noble metal substrates typically require complicated and delicate fabrication procedures which makes them less controllable and reproducible. Furthermore, they suffer from the excessive cost, low surface uniformity, photobleaching effect, poor biocapability, and so on. Another SERS theory is the chemical mechanism (CM) that originates from the charge transfer between the SERS substrate and the probe molecules. The CM makes the molecule more polarized, so as to increase the Raman scattering cross-section. However, traditionally it is

Received: March 16, 2018
Published: June 21, 2018

DOI: 10.1021/jacs.8b02972
J. Am. Chem. Soc. 2018, 140, 8696−8704

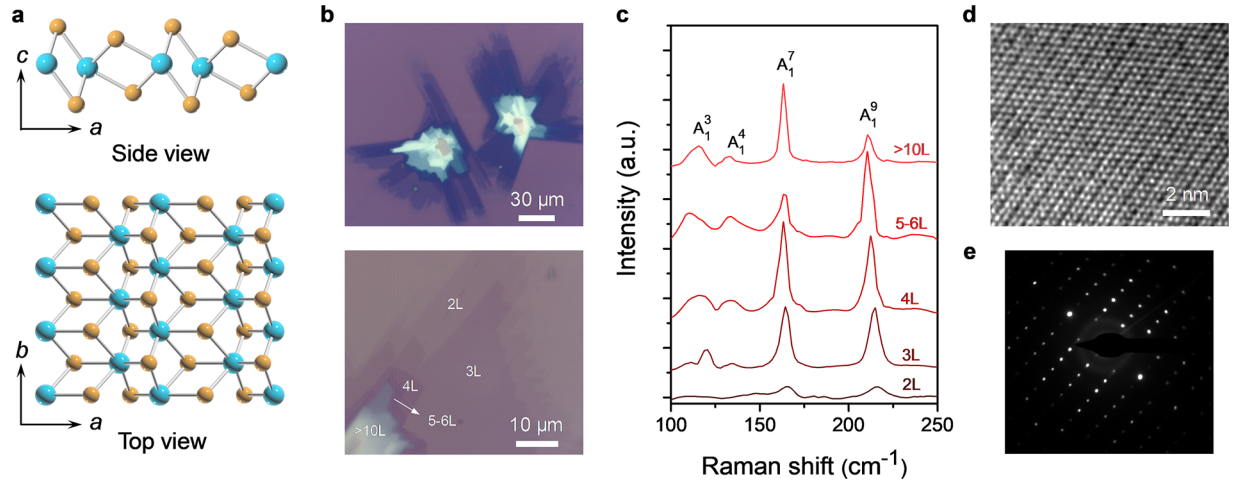

Figure 1. Characterization of the 1T′ transition metal telluride atomic layers. (a) Side and top views of lattice structures of monolayer 1T′ transition metal tellurides. Brown spheres: tellurium atoms. Blue spheres: transition metal atoms. (b) Optical images of the 1T′-WTe_2 atomic layers. The layer number n was indicated with nL. (c) Raman spectra of 1T′-WTe_2 flakes with various layer numbers. (d, e) High-resolution TEM (d) and SAED (e) images of the 1T′-WTe_2 atomic layers.

believed that the CM is less responsible for the total enhancement (comparing with the EM) since this process is a short-range one.[6−8]

The past few decades have witnessed the discovery and advances of noble-metal-free SERS mediators based on CM, such as nanostructured semiconductors (e.g., ZnO, Cu_2O, and α,ω-diperfluorohexylquaterthiophene).[9−11] The family of two-dimensional (2D) layered materials (e.g., graphene and MoS_2), as a rising star in optoelectronics,[12−14] has been recently entered the game of Raman enhancer.[15−21] The 2D atomic layers are suggested to be promising candidates for the next-generation SERS substrates due to their atomic uniformity, chemical stability, and biocapability. However, the Raman enhancement factors (EFs) and the limits of detection (LODs) of 2D SERS materials are still greatly inferior to the noble metal structures. Hence, it is of crucial importance to pursue more powerful 2D materials as SERS substrates. The interaction between the SERS substrate and the analyte plays the key role in the CM contributed Raman enhancement. Generally, highly desirable charge transfer between the SERS substrate and the analyte requires the SERS material surface to be flat and active to chemisorb the molecules.[22,23] Furthermore, the band alignment of the analyte-SERS material interface and the available energy levels (density of states, DOS) of the SERS material should be favorable for the charge transfer processes.[17]

Recently, 1T′ transition metal telluride semimetals (e.g., WTe_2 and $MoTe_2$) have attracted a tremendous amount of attention due to their intriguing physical properties such as the type-II Weyl semimetal nature and the extremely large magnetoresistance.[24−26] More importantly, their relatively high surface activities and large DOS near the Fermi levels imply that the 1T′ transition metal tellurides can provide strong analyte-SERS material coupling and effective charge transfer, and may become ideal 2D SERS materials. Furthermore, large-area few-layer 1T′ transition metal telluride flakes are attainable through facile chemical vapor deposition (CVD) processes, which facilitates their development for practical SERS applications.[27,28] Herein, we report CVD-obtained large-scale 1T′ transition metal telluride atomic layers as SERS substrates performing extremely large Raman enhancement. As a proof of concept, the limit concentration of detection of a typical dye analyte Rhodamine 6G (R6G) on 1T′-W(Mo)Te_2 can be as low as 10^{-15} (10^{-14}) M and the Raman EF reaches a noble-metal-comparable one of 10^{10} (10^9). The capability of the 1T′-W(Mo)Te_2 as a versatile SERS substrate was further confirmed with various analytes other than R6G, and the SERS detection is stable both to air aging and to laser illumination. In addition, the efficient fluorescence (FL) quenching of analyte on 1T′-WTe_2 was simultaneously detected, allowing the Raman signals to be outstanding among the backgrounds. Microtransmission measurements and density functional theory (DFT) simulation results, as well as the mentioned FL suppressing, all support the theory of CM by illustrating the fact that the strong analyte-telluride interaction gives rise to the large charge transfer between them by efficiently borrowing the intensity from the nearby molecular optical transition.[6]

RESULTS AND DISCUSSION

Characterization of the 1T′ Transition Metal Tellurides. The large-area 1T′ transition metal telluride atomic layers (crystal structures shown in Figure 1a) with high-quality were obtained via a facile, low-cost, and robust CVD strategy, of which the growth details are available in our previous report.[28] The vital issue in the synthesis procedure is that the ordinary salts like KCl added in the tellurium precursor can vastly promote the tellurization, whereas the reaction is normally suppressed by the low chemical activity of tellurium. Figure 1b reveals that our CVD process guarantees high-density deposition of few-layer WTe_2 flakes with large scales (~110 μm) on a SiO_2/Si substrate. The optical contrast can roughly indicate the layer numbers of the as-grown WTe_2 (Figure 1b), as will be evidenced by the following. Atomic force microscope (AFM) measurements were conducted to directly probe the thickness. The hierarchically layered morphologies along with the detailed step height profiles of a typical thickness-varied WTe_2 flake in Figure S1a can identify the layer numbers, with consideration that a monolayer WTe_2 is ~1 nm.[29] Raman spectra of the WTe_2 flakes with various thicknesses are presented in Figure 1c. Four fingerprint phonon modes of 1T′-WTe_2, i.e., A_1^3, A_1^4, A_1^7, and A_1^9, are

DOI: 10.1021/jacs.8b02972
J. Am. Chem. Soc. 2018, 140, 8696−8704

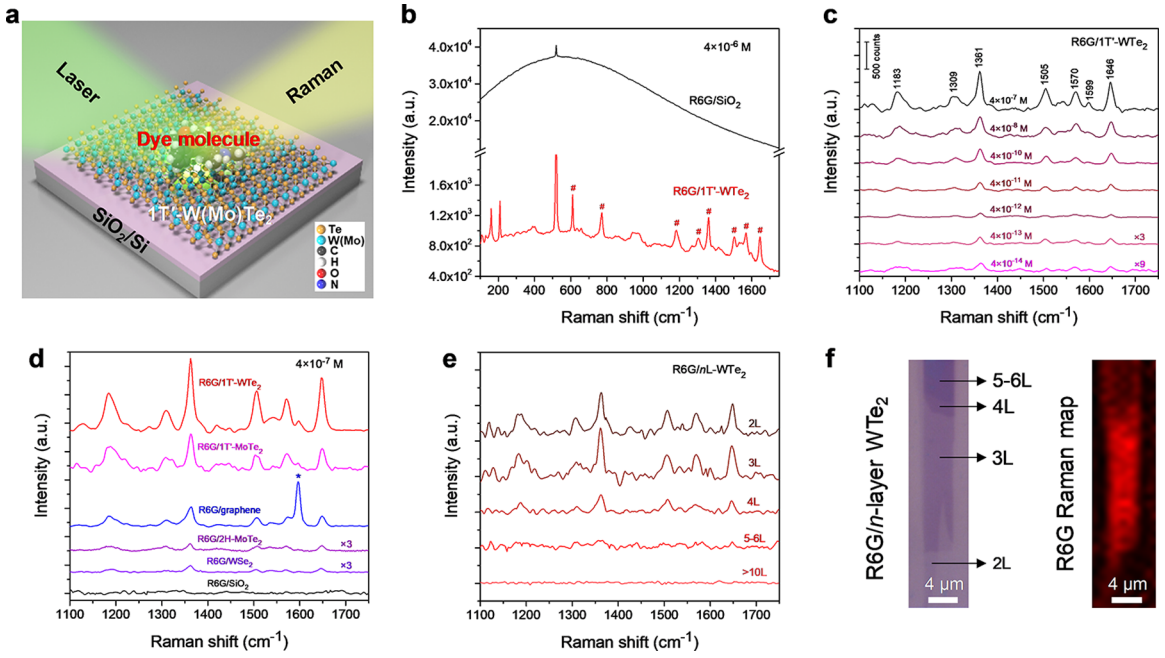

Figure 2. FL quenching and SERS effects on the 1T′ transition metal tellurides. (a) Schematic diagram of the 2D transition metal tellurides as platforms for FL quenching and Raman enhancing of analytes. (b) Raman-FL spectra of the dye R6G coated on bare SiO_2 (black line) and on 2D 1T′-WTe_2 (red line). The signal integration times were 0.5 s for the black line and 4 s for the red line, respectively. The plotted intensities are normalized with respect to the integration times. The Raman peaks labeled with "#" denote the R6G signatures. (c) SERS spectra of R6G coated on 1T′-WTe_2 flakes (3L) with various concentrations from 4×10^{-7} to 4×10^{-14} M. (d) Raman spectra of R6G coated on 2D 1T′-WTe_2, 1T′-$MoTe_2$, graphene, 2H-$MoTe_2$, WSe_2, and bare SiO_2 substrates with a fixed concentration of 4×10^{-7} M. The Raman peak labeled with "*" is from graphene G mode. (e) Raman spectra of R6G (4×10^{-8} M) coated on 1T′-WTe_2 flakes having various layer numbers. Acquisition time for each spectrum is 2 s. (f) Optical image and the corresponding Raman intensity map at R6G 1646 cm^{-1} peak of the layer-varied 2D 1T′-WTe_2 with R6G deposition.

observed, and the latter two give more prominent intensities.[29] It is noteworthy that the main Raman signatures of 2D WTe_2 lie in the range of 100−250 cm^{-1}, which are far away from the Raman-active region of most common dye analytes (500−1800 cm^{-1}). This Raman-silent feature of WTe_2 can largely avoid the unwanted Raman interference in SERS demonstration. The WTe_2 A_1^9 mode is related to the out-of-plane vibration of WTe_2 and is sensitive to the layer number.[29] As the thickness of WTe_2 flakes increases from bilayer (2L) to more than ten-layers (10L), the A_1^9 phonon performs a red shift from 216.1 to 211 cm^{-1} (Figure S1b, SI).

The crystalline microstructures of the WTe_2 were further studied through transmission electron microscopy (TEM). A typical high-resolution TEM image displayed in Figure 1d shows the distorted 1T (1T′) phase atomic arrangement along zone [001] axis. The tungsten layer on the top is shifted with respect to the bottom one, forming an ABC stack of the W−Te−W three-atomic-layer. The selected area electron diffraction (SAED) pattern in Figure 1e further demonstrates the rectangular symmetry of 1T′-WTe_2 with space group $P2_1/m$.[30] The 1T′ phase is a metastable one for most group-VI transition metal dichalcogenides, whereas the WTe_2 is an exception of which ground state is 1T′.[12,18,31] Additionally, the CVD-derived WTe_2 few-layer films are very air-durable.[27,28] As evidenced by the Raman spectroscopy in Figure S1c, the as-synthesized WTe_2 few-layer flakes shows no obvious degradation under ambient conditions for one month (Figure S1d,e). Raman intensity maps and AFM images further evidence the promising stability of the few-layer WTe_2 upon air aging (Figure S1f−i). The phase and air stabilities of the 1T′-WTe_2 are essential for a feasible SERS material toward real applications. 2D 1T′-$MoTe_2$ flakes were also synthesized, as characterized in Figure S1j,k.

Molecular Fluorescence Quenching and Raman Enhancement on 1T′ Transition Metal Tellurides. To investigate the SERS performance of the sizable 1T′ transition metal tellurides, we first applied a typical dye molecule R6G as the Raman probe. Figure 2a schematically illustrates the probe molecules on 1T′ tellurides for SERS experiments. The R6G solution (4×10^{-6} M) was drop-casted (see Methods for details) on the 1T′-WTe_2 and the Raman-FL spectra (excitation wavelength 532 nm) without baseline correction taken from regions with and without trilayer (3L) WTe_2 flakes are given in Figure 2b. The signals collected from the bare SiO_2 substrate with R6G deposition exhibit large FL background while no detectable Raman peaks can be found. The immense FL that overwhelms the Raman signals is a major obstacle in resonance Raman spectroscopy which limits its further development.[32] The results for R6G on WTe_2, however, show enormously suppressed FL by a factor of ∼40 and enhanced Raman features of the dye labeled with "#" that can be discerned clearly. The efficient charge transfer between WTe_2 and R6G triggers the decreasing of FL cross-section and the consequent FL quenching. With the adoption of 1T′-WTe_2 atomic layers, the signal ratios of Raman/FL features are greatly augmented, allowing the analyte Raman peaks to be distinguishable from the background.

The SERS technique is of great interest for probing trace amounts of molecules. We prepared a set of R6G solutions with gradually decreased concentrations down to 4×10^{-15} M (4 fM) (photographs are available in Figure S2) to study the sensitivity of the SERS-active WTe_2 atomic layers. Figure 2c displays the Raman spectra of R6G/3L-WTe_2 with various

DOI: 10.1021/jacs.8b02972
J. Am. Chem. Soc. 2018, 140, 8696−8704

concentrations. Conspicuous R6G Raman signatures positioned at 1183, 1309, 1361, 1505, 1570, 1599, and 1646 cm^{-1} are labeled, consistent with the literature.[15,22] The results are highly reproductive as evidenced by taking Raman spectra from 20 randomly chosen spots on the WTe_2 flake (Figure S3a). The characteristic spectra are nearly identical concluding the uniformity of the WTe_2-induced SERS, which is attributed to the atomically flat surface of 2D WTe_2. The crystal structure of 1T′-WTe_2 was not modified by R6G adsorption, as demonstrated in Raman spectra in Figure S3b. The Raman intensity of R6G 1646 cm^{-1} feature as a function of concentration is shown in Figure S3c. The supersaturated adsorption was not observed since at low concentrations ($<10^{-6}$ M), the adsorbed dye molecules formed a submonolayer without clustering.[15,17] At an ultralow concentration of 4×10^{-14} M, the fingerprint Raman bands were still detectable (a single spectrum is shown in Figure S3d), with a reasonable signal-to-noise ratio (8.4 for 1646 cm^{-1} peak). This remarkable LOD enables 1T′-WTe_2 to be an ultrasensitive platform for SERS. The corresponding Raman EF was calculated to be 1.8×10^9 taking bulk analyte as the reference (Figure S4). It is inspiring that the pristine 2D 1T′-WTe_2 without any further doping or structural modification presents promising SERS-active characteristic which is superior to the reported semiconductors and 2D materials and is even comparable to SPR-based noble metals as Raman enhancement mediators. The 1T′-$MoTe_2$ atomic layers delivers ultrasensitive SERS performance as well (Figure S3e,f), presenting a remarkable LOD of 4×10^{-13} M and Raman EF of 1.6×10^8 for R6G probe. A detailed comparison of the SERS performance (LOD and/or EF) between the demonstrated transition metal tellurides and some other results from the references is summarized in Table S1.

We also conducted a set of control experiments to directly compare the Raman enhancement effects of 1T′-W(Mo)Te_2 and diverse 2D materials beyond it, i.e., CVD-derived monolayer graphene and WSe_2, and bilayer 2H-$MoTe_2$ as well (characterization is provided in Figure S5).[28,33] Figure 2d concludes the Raman spectra collected on the above-mentioned materials and bare SiO_2 as well, with R6G dye (4×10^{-7} M) deposited via identical process. It is obvious that 1T′-W(Mo)Te_2 produces much larger Raman enhancement than graphene, while the dye is not detectable on bare SiO_2. In addition, graphene itself has interference Raman features (G peak at 1582 cm^{-1} and the possible D peak at 1345 cm^{-1})[34] to the analyte signals which is detrimental for SERS. When the dye concentration goes to a lower one of 4×10^{-10} M, there is no observable Raman signals from the analyte on graphene whereas the SERS effects are still remarkable on 1T′-W(Mo)Te_2 (Figure S6). WSe_2 shows limited capability of Raman enhancement in comparison with semimetallic tellurides and graphene, although it is reported to be better than other semiconducting 2D materials like MoS_2.[35] Interestingly, the semiconducting 2H-$MoTe_2$ presents SERS effects which are much lower than its 1T′ counterpart, indicating that the material's phase generates significant impacts on the Raman enhancement, similar to those on the catalytic activity.[36] Our present work suggests that the 1T′ transition metal tellurides as new SERS materials are much more promising than the intensively discussed graphene, not only showing superior LODs and EFs, but also resolving the problem of Raman peak interference. In comparison to graphene, the strongly coupled analyte-telluride surface and the large low-energy DOS which accelerates the charge transfer in combination delivers the outstanding SERS effects of 1T′ transition metal tellurides, as we will discuss later.

Another interesting topic is to discuss the influence of WTe_2 layer number on the Raman enhancement effect. Figure 2e gives the Raman spectra of R6G (4×10^{-8} M) coated on WTe_2 having various layer numbers and Figure S7 lists the Raman intensity of an R6G characteristic peak 1646 cm^{-1} as a function of the WTe_2 layer number. On 2L and 3L WTe_2, the Raman intensities of dye were very similar, with the latter being slightly higher. As the thickness of WTe_2 further increases, the R6G Raman signal intensity dramatically reduces, and eventually becomes undetectable on a thick film (>10L or bulk). Figure 2f presents the Raman intensity map of 1646 cm^{-1} band on a typical layered WTe_2 flake corresponding to the optical image. The Raman intensity contrasts on the studied area vividly depict the intensity distribution that the analyte signal gets weaker on thick WTe_2. The overall decreasing trend of the dye Raman signal with the SERS material getting thicker has been observed in other layered 2D materials.[35,37,38] On the basis of the multilayer Fresnel system, the field intensity of dye coated on a 2D film becomes lower with the increasing layer number, which delivers the suppressing of the dye Raman intensity.[35] Other mechanisms, such as the layer-dependent bandstructure of the 2D material, substrate induced doping and the chemisorption capability of the film with different thicknesses, may also contribute to the total Raman enhancement.[15,37,38] Further survey is still needed to fully understand the thickness dependence effect.

The strong SERS effect on 1T′ transition metal tellurides is a universal phenomenon for a diverse range of dyes beyond R6G, such as crystal violet (CV) and rhodamine B (RhB). Among them, CV is a prohibited fish drug, which may pose health risks and adverse environmental impact.[39] Figure 3a,b give representative Raman spectra of dyes CV and RhB coated on 3L-WTe_2, respectively. The Raman results at the dye concentration of 4×10^{-7} M exhibit substantial signatures of each analyte which are labeled with peak positions.[17,38] When going to ultralow dye concentrations (4×10^{-13} M for CV and 4×10^{-12} M for RhB), the characteristic Raman peaks of the probe molecules were still distinguishable from the noise, evidencing the ultrahigh SERS sensitivity of the demonstrated 1T′-WTe_2 for various probes. The demonstrated SERS has promising applications in the fields of food safety, environmental protection, and so on.

The stability of SERS measurements, both in long-term and short-term, is also a pivotal issue toward the application. Figure 3c plots the evolution of in situ Raman spectra of R6G dye (4×10^{-8} M) deposited on WTe_2 with exposure to ambient and Figure S8 gives the Raman intensities of R6G feature peaks 1361 and 1646 cm^{-1} versus the exposure time. The dye signals show limited degradation in ambient air during the surveyed period of 12 days, evidencing the reliable SERS effects on 1T′-WTe_2 against air exposure. This is attributed to not only the satisfactory air stability of the CVD-grown WTe_2 as mentioned before, but also the robust adsorption of the analytes on WTe_2. Photoinduced analyte structural damage caused by photobleaching and/or metal-catalyzed side reaction is a severe drawback of the conventional SERS substrates based on SPR.[5,40,41] The noble-metal-free WTe_2 SERS platform can mostly avoid this irreversible damage to the Raman probes. We have fabricated a SERS substrate consisting of random gold nanoislands (AuNIs) for comparatively studying the photo-

DOI: 10.1021/jacs.8b02972
J. Am. Chem. Soc. 2018, 140, 8696−8704

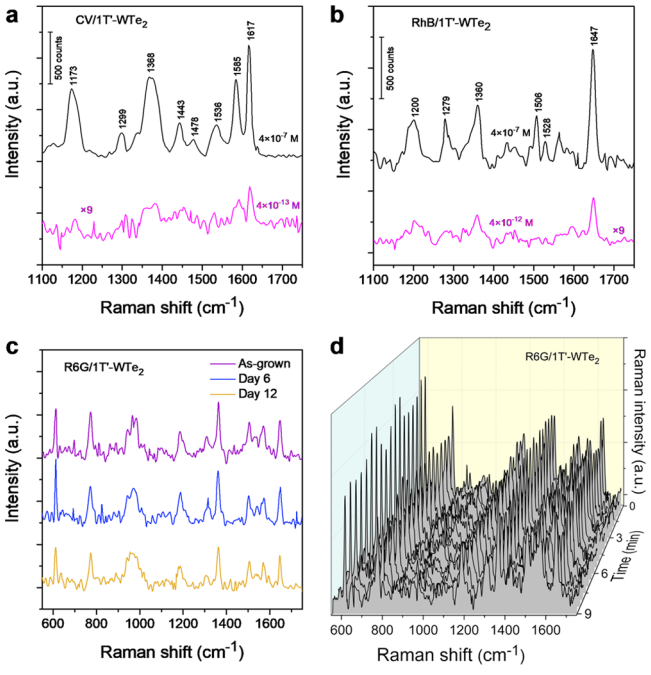

Figure 3. Universal capability and stability of the 1T′-WTe_2 as SERS material. (a, b) SERS spectra of dyes CV (a) and RhB (b) deposited on 1T′-WTe_2 atomic layers with various concentrations. (c) Evolution of Raman spectra of R6G (4×10^{-8} M) coated on 2D 1T′-WTe_2 after aging in ambient for up to 12 days. Acquisition time for each spectrum is 2 s. (d) Photostability of the SERS spectra of R6G/1T′-WTe_2 (4×10^{-7} M concentration) in a period of 9 min. Each of the 18 spectra was acquired with an integration time of 10 s.

degradation effects.[42] A typical scanning electron microscope (SEM) image of the AuNI substrate can be found in Figure S9a. Figures 3d and S9b are the time-dependent Raman spectra of the R6G probe (4×10^{-7} M) on WTe_2 flakes and on the AuNI substrate, respectively. Each Raman spectrum was obtained with 10 s acquisition time followed by a fixed interval before the next measurement. It is concluded that the decrease of dye Raman intensity on WTe_2 is limited, whereas the Raman signals show apparent degradation on AuNIs over the measuring time (Figure S9c). Similar results were also found in graphene-based SERS demonstration,[41,43] indicating that the photostability is a common advantage of the SPR-free SERS candidates over noble metals. This stabilization is believed to origin from the large charge transfer between the analyte and WTe_2, which facilitates the charge relaxation from the analyte excitation states.[43]

Charge Transfer Mechanism of the Large Raman Enhancement. The EM contribution is excluded in the WTe_2-induced SERS effect, since the SPR of WTe_2 is at the mid-infrared regime (Supplementary Note S1). The SPR-free feature at the Raman excitation wavelength was further confirmed by investigating the reflection spectrum and the near-field nano-optical properties of the 2D 1T′-WTe_2 (Figure S10). Microtransmission measurements were performed to examine the interaction between the analyte and the 2D 1T′-WTe_2. As shown in Figure 4a, an additional absorption band around 519−574 nm was observed in the transmission spectrum (red curve) of R6G dye (4×10^{-7} M) coated on WTe_2/quartz with respect to the case of pristine WTe_2/quartz (blue curve), which can be assigned to the contribution of R6G absorption (see the transmission spectrum of bulk R6G in Figure S11a). On the contrary, the R6G absorption peaks were not detectable on the dye coated quartz substrate due to the absence of analyte-substrate coupling (gray curve in Figure 4a). The enhancement of dye absorption on WTe_2 surface indicates the efficient charge transition probability between the dye molecule and WTe_2, which is also believed to be the key origin of the large SERS effect of WTe_2.[16,22,44] Note that the dye absorption is hardly detected in graphene coated with R6G, as shown in Figure S11b, indicating that the charge transfer in R6G-telluride is much larger than that in R6G-graphene. This is consistent with the fact that graphene is chemically inert while semimetallic tellurides have much enhanced activities. The coupling of R6G and WTe_2 as well as the consequent charge transfer at equilibrium were investigated by DFT calculations, as illustrated in Figure 4b,c. The DFT results show that the binding energy of R6G-WTe_2 is 0.67 eV and the electron transfer from WTe_2 to R6G is 1.26 e/molecule, while for the R6G-graphene complex, the binding energy and the electron transfer are only 0.24 eV and 0.46 e/molecule, respectively. The binding energy and the value of charge transfer reveal that the coupling of R6G-WTe_2 is much stronger than that of R6G-graphene. Furthermore, from the charge density isosurfaces, it is found that for the R6G-graphene complex, the electrons and holes generated by charge transfer are closely located around the graphene surface and R6G molecule, respectively, forming a dipole at the interface. The dipole prompts the SERS effects of dye on graphene. For the R6G-WTe_2 system, the interface dipole is much stronger than that at R6G-graphene due to the larger number of charge transfer. More importantly, because of the relatively high surface activity of 1T′ telluride, the transferred charges are collected between WTe_2 and R6G molecule, resulting in a "quasi-covalent bonding" in the R6G-WTe_2 complex, which will strengthen the coupling between R6G and WTe_2 beyond dipole electrostatic force, and thus further increase the Raman scattering cross-section of the dye molecule. Therefore, the large dipole and "quasi-covalent bonding" in combination brings about the outstanding SERS performance of 1T′ transition metal tellurides. Note that the surface oxidation which occurs at the Te vacancy sites has limited influence on the calculated results.[45] The excessive Te supply in the CVD process minimizes the formation of Te vacancies, and the residual intact surface Te atoms guarantee the strong analyte-telluride coupling.

In addition to the static coupling of analyte and SERS mediator discussed above, the realistic SERS effects on 1T′ transition metal tellurides originate from the photoinduced charge transfer (PICT) driven CM, as illustrated in Figure 4d. The highest occupied molecular orbital (HOMO) and lowest unoccupied molecular orbital (LUMO) levels of R6G probe are −5.7 and −3.4 eV, respectively,[15] and the Fermi level of 1T′-W(Mo)Te_2 is determined to be −4.52 eV (−4.59 eV) by Kelvin probe force microscopy (KPFM) as shown in Figure S12. The PICT transitions from both the R6G HOMO to the telluride Fermi level and the telluride Fermi level to the R6G LUMO in the coupled complex are responsible to the total Raman enhancement,[6,46] resulting from the broad charge transfer resonance energy range.[47] These resonances borrow the intensity from molecular transition through a vibronic coupling Herzberg−Teller process, thus largely magnifying the polarization tensor of the probe.[6,48] Moreover, the nearly symmetrical match of the 1T′-W(Mo)Te_2 Fermi level to the molecular HOMO and LUMO further facilitates the PICT.[15]

DOI: 10.1021/jacs.8b02972
J. Am. Chem. Soc. 2018, 140, 8696−8704

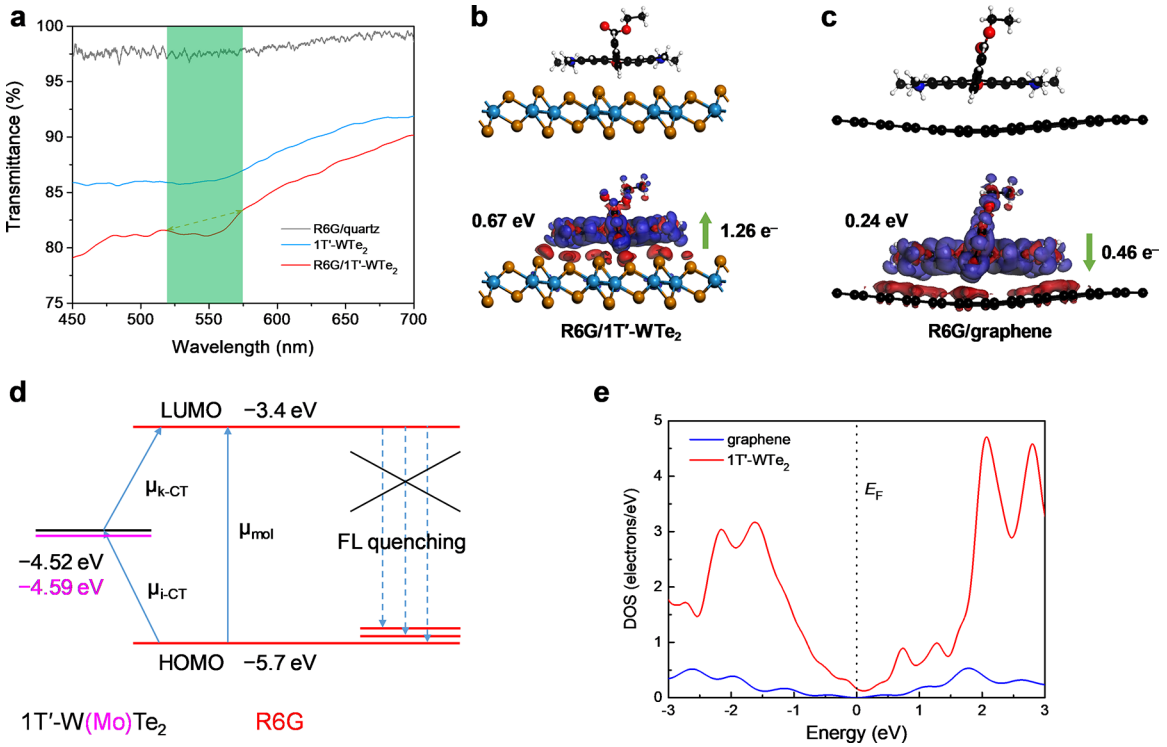

Figure 4. Chemical mechanism of the SERS effect. (a) Transmission spectra of 1T′-WTe_2 and R6G (4×10^{-7} M) coated 1T′-WTe_2 and quartz. The dashed box denotes the R6G absorption band. (b, c) Side views of the electron density difference isosurfaces for R6G chemisorbed onto the 1T′-WTe_2 (b) and graphene (c). Blue and red colors correspond to electron depletion and accumulation regions, respectively. The arrows indicate the direction of electron transfer. The binding energies of R6G-SERS mediators are labeled. (d) Energy level diagram and charge transfer transitions in the R6G-W(Mo)Te_2 complex. μ_{mol} denotes the molecular transition. μ_{i-CT} and μ_{k-CT} denote the charge transfer transitions from the molecular ground states $|i\rangle$ to W(Mo)Te_2 and from W(Mo)Te_2 to the molecular excited states $|k\rangle$, respectively. (e) The density of states (DOS) of 1T′-WTe_2 and graphene near the Fermi levels.

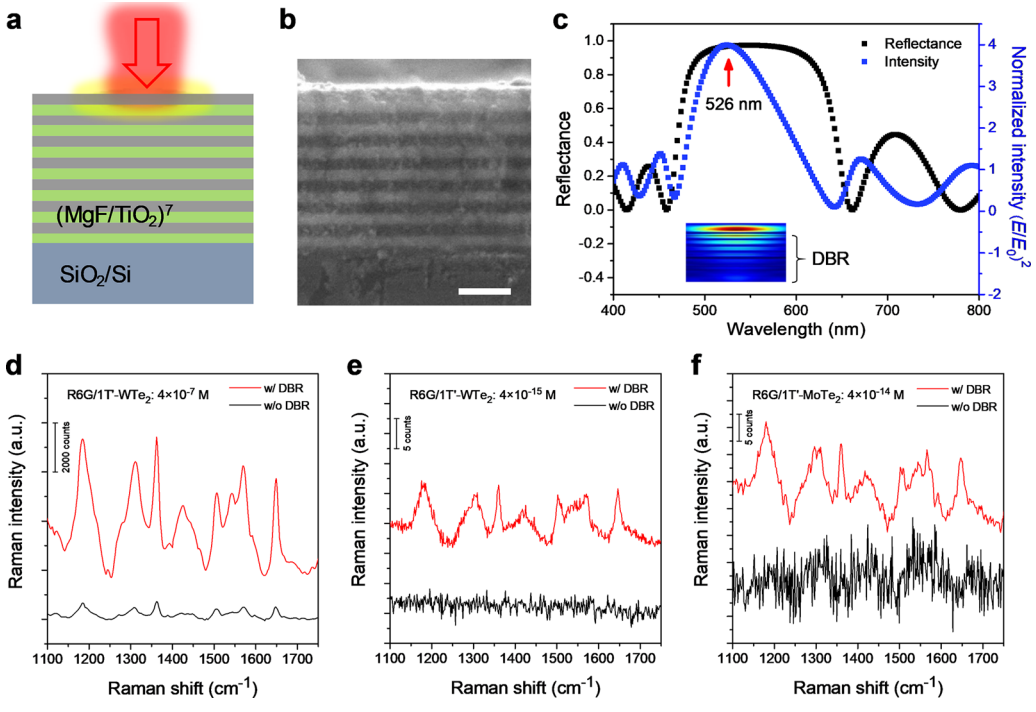

Figure 5. Further Raman enhancement by the Bragg reflector. (a, b) Schematic (a) and cross-sectional SEM image (b) of the DBR adopted for light field enhancement. Scale bar: 400 μm. (c) Calculated reflection spectrum of the DBR and normalized intensity $(E/E_0)^2$ at the surface of DBR. Inset is the field distribution at the wavelength of 532 nm. (d) SERS spectra of 4×10^{-7} M R6G coated on 1T′-WTe_2 with and without DBR integration. (e) Raman spectra of 4×10^{-15} M R6G coated on 1T′-WTe_2 with and without DBR integration. (f) Raman spectra of 4×10^{-14} M R6G coated on 1T′-$MoTe_2$ with and without DBR integration.

DOI: 10.1021/jacs.8b02972
J. Am. Chem. Soc. 2018, 140, 8696−8704

The large number of allowed energy states for PICT in 1T′-WTe_2 (DOS near the Fermi level, see Figures 4e and S13) further gives rise to the high charge transition probabilities (w) according to the Fermi's golden rule: $w_{ab} = \frac{2\pi}{\hbar}|\langle b|M|a\rangle|^2 g_b$, where $|a\rangle$ and $|b\rangle$ denote the initial and final states for the charge transition, $\hbar$ is the reduced Planck constant, M is the interaction operator of the two states, and g_b is the DOS of the final state. In addition to the charge transfer resonances, the molecular resonance at 532 nm excitation augments the cross-section of probe Raman scattering as well.[49] As demonstrated in Figure S14, the Raman spectra show prominent SERS effects at 532 nm excitation, while no detectable SERS signals are collected under laser wavelengths of 633 and 785 nm. In general, the polarization tensor is expressed as $\alpha = A + B + C$, where A is relevant to molecular resonance, and B and C represent the two charge transfer resonances.[46] Molecular FL quenching is another consequence of the large charge transfer in the analyte-WTe_2 system, as illustrated in Figure 4d. It is worth noting that the charge transfer resonances are expected to be largely enhanced when vibronically coupled with the molecular resonance, with the degree highly relevant to the analyte-telluride interaction. CM has been considered to be a secondary or even negligible factor in the total Raman enhancement in noble-metal-based SERS substrates.[50] In our demonstrated results, however, it is shown that the Raman enhancement contributed by charge transfer resonances that borrow the intensities from the dye molecular resonance can reach excellent levels of LOD and EF which are comparable to noble metals where EM is dominating, shedding new light on the CM enabled SERS effect. The immense CM-driven Raman enhancement stems from the strong coupling of the analyte-1T′ telluride system and the large available DOS of the semimetal telluride that accelerates the charge transfer resonances.

Further Improvement of Raman Enhancement by Bragg Reflector. The above results have demonstrated the ultrasensitive Raman enhancement of the intrinsic 1T′-W(Mo)Te_2 atomic layers. The phenomenal Raman enhancement could be further improved by integrating certain optical structures that promote the light field localization on the SERS material. We have designed and fabricated a distributed Bragg reflector (DBR) as the field enhancer for 1T′-W(Mo)Te_2 to explore whether the SERS effect could be amplified (Figure 5a).[51] The DBR consists of alternating MgF and TiO_2 layers (both with a thickness of 80 nm) grown atop a SiO_2/Si substrate, with the cross-sectional SEM image given in Figure 5b. Typical reflection spectrum of the DBR is shown in Figure 5c, unveiling a photonic bandgap ranging from 480 to 610 nm. Notably, the field intensity at the surface of the DBR receives a maximum enhancement by the factor of ∼4 at the wavelength of 526 nm (close to the 532 nm Raman excitation). Also, the field distribution under 532 nm illumination (inset of Figure 5c) reveals that the electromagnetic field is highly localized at the surface.

The WTe_2 sheets were transferred onto the DBR substrate via the conventional wet etching processes. Raman spectra in Figure S15 indicate that the quality of the WTe_2 was highly preserved during the transfer (onto a new SiO_2/Si substrate). By incorporating with the exquisitely designed DBR, the Raman enhancement of the 2D WTe_2 can be largely augmented, as shown in Figure 5d. Compared to the case of R6G/WTe_2 on SiO_2/Si, the Raman features of analyte R6G (4×10^{-7} M) deposited on WTe_2 with underlying DBR present amplified intensities with the factor of ∼7.3 (for 1646 cm^{-1} peak). The employment of DBR allows the detection of lower concentration of analyte on the WTe_2 surface even with one order weaker excitation power (0.1 mW, see Methods). Figure 5e depicts the SERS spectrum of R6G with 4×10^{-15} M coated on the WTe_2/DBR structure. The main Raman signatures of the femtomolar R6G analyte were clearly identified. This ultralow LOD delivers an ultrahigh Raman EF as well, up to 4.4×10^{10} (Figure S4). The SERS measurements on R6G/1T′-$MoTe_2$ integrated on the DBR structure were demonstrated in Figure 5f, presenting a promising LOD of 4×10^{-14} M along with the corresponding Raman EF of 6.2×10^9. It is worth noting that we did not introduce any noble metals that generate SPR hot spots in the further enhancement, which avoids the mentioned drawbacks of noble-metal-based SERS materials such as photobleaching and low biocapacity. We demonstrate that a SPR-free SERS structure (WTe_2 integrated on DBR) can reach a femtomolar level detection of probe molecules, which is comparable with or even superior to the SPR-based complicated structures. The large CM contribution of the analyte−telluride complex combined with the promoted field localization by DBR results in the prominent SERS effect.

CONCLUSIONS

We demonstrate that the CVD-grown 1T′-W(Mo)Te_2 atomic layers are promising candidates for CM-based (SPR-free) SERS and FL quenching. The limit concentration of detection of dye R6G coated on 1T′-W(Mo)Te_2 integrated on Bragg reflector can achieve femtomolar levels, and the Raman EF can be larger than 10^{10} (10^9). The outstanding SERS effects on 1T′-W(Mo)Te_2 far exceed the previously reported CM-based SERS mediators such as semiconducting thin films and 2D materials like graphene. More importantly, we reveal that CM-based SERS materials can approach Raman enhancement effects that are comparable or even superior to the noble metal structures based on SPR. Experimental and DFT simulated results unveil that the ultrasensitive SERS effects on 1T′-W(Mo)Te_2 rely on the strong analyte−telluride interaction and the large DOS near the Fermi level of the telluride type-II Weyl semimetals. Our results bring the 1T′ transition metal telluride atomic layers for ultrasensitive SERS detection without introducing noble metals, and offer new insights into the CM-based charge transfer processes in SERS effects.

METHODS

CVD Growth and Characterization of 1T′ Transition Metal Telluride Atomic Layers. The 30 mg mixture of ammonium tungstate hydrate (ammonium molybdate tetrahydrate) and KCl with the mass ratio of $(NH_4)_{10}W_{12}O_{41}{\cdot}xH_2O$ ($(NH_4)_6Mo_7O_{24}{\cdot}4H_2O$):KCl = 10:1 as W(Mo) precursor was placed into a corundum boat. A freshly cleaned SiO_2/Si substrate was mounted on the top of the corundum boat, and the Te powder (60 mg) was placed upstream. The system was ramped to 800 °C within 17 min, and remained at 800 °C for the growth of 1T′-W(Mo)Te_2 for 5 min under atmospheric pressure with a mixture of argon and hydrogen (20% H_2), at a flow rate of 250 sccm. When the growth was terminated, the sample was rapidly cooled down to room temperature. TEM measurements were performed with FEI Tecnai F20. AFM and KPFM experiments were conducted with Bruker Dimension Icon.

SERS Measurements. Ethanol solution of dye molecules (R6G, CV and RhB) having different concentrations were obtained via sequential diluting processes. For each SERS measurement, 10 μL probe solution was dropped on the SERS-active material on the

DOI: 10.1021/jacs.8b02972
J. Am. Chem. Soc. 2018, 140, 8696−8704

substrate followed by a gentle dry process. The substrate was then rinsed in absolute ethanol 3 times to remove the free molecules and was ready for Raman measurements. All the Raman measurements were taken with a HORIBA LabRAM HR Evolution system having a laser spot size of ~1 μm. The excitation wavelength is 532 nm, and the laser power was set at 1 mW unless specified. The SERS spectra were obtained with 40 s acquisition time unless specified. For SERS measurements at ultralow dye concentrations ($<10^{-12}$ M), we collected the average intensities among 10 single spectra taken on identical positions to minimize the signal noise. The spectra for comparison were acquired under identical measuring conditions. The laser power was set at 0.1 mW when performing SERS experiments on the DBR. Baseline correction has been done in the SERS spectra except for the demonstration of FL quenching in Figure 2b. Raman mapping was conducted with spatial steps of 0.5 μm, and the acquisition time for each point is 1 s.

DFT Calculations. All calculations were performed using the Perdew–Burke–Ernzerhof (PBE) formulation of the generalized gradient approximation (GGA) with the projected augmented wave (PAW) potentials were used with a kinetic energy cutoff of 450 eV, as implemented in the Vienna ab initio Simulation Package (VASP). The Brillouin zone integration was sampled by a 2 × 2 × 1 k mesh. The systems were simulated with a periodic boundary condition by placing an R6G molecule on the surface of 144-atom WTe_2 (W:48 and Te:96) and 216-atom graphene sheets, respectively. The geometry was fully relaxed without any constraint until the force on each atom was less than 0.01 eVÅ^{-1}. The adsorption energy for R6G adsorbed on WTe_2 (graphene) was calculated using $E_a = E_{WTe2}(E_g) + E_{R6G} - E_{system}$, where $E_{WTe2}(E_g)$, E_{R6G}, and E_{system} are the energies of WTe_2 (graphene), an R6G molecule, and the combined system of them, respectively.

■ ASSOCIATED CONTENT

Supporting Information

The Supporting Information is available free of charge on the ACS Publications website at DOI: 10.1021/jacs.8b02972.

Additional characterization, data and analysis including Figures S1–S15 and Supplementary Note S1 (PDF)

■ AUTHOR INFORMATION

Corresponding Authors

*E-mail: chenk69@mail.sysu.edu.cn (K.C.).
*E-mail: jbxu@ee.cuhk.edu.hk (J.-B.X.).

ORCID

Li Tao: 0000-0002-7757-1149
Zefeng Chen: 0000-0002-0689-8443
Chunxiao Cong: 0000-0001-9786-825X
Huanjun Chen: 0000-0003-4699-009X
Weiguang Xie: 0000-0002-3706-6359
Jian-Bin Xu: 0000-0003-0509-9508

Author Contributions

These authors contributed equally to this work.

Notes

The authors declare no competing financial interest.

■ ACKNOWLEDGMENTS

The authors are thankful to Mr. Junling Xu for fruitful discussion. J.X. thanks the support by RGC of Hong Kong (AoE/P-03/08, AoE/P-02/12, 14207515, and 14204616), CUHK Group Research Scheme, ITC (ITS/088/17), and the NSFC (61229401). K.C. acknowledges the support by the Hundred Talents Plan of Sun Yat-Sen University (76120-1882110). W.X. thanks the support from the NSFC (11574119). T.Y. thanks the support by Start-up grant M4080513. C.C. thanks the support by the NSFC (61774040), the National Young 1000 Talent Plan of China, and the Shanghai Municipal Natural Science Foundation (16ZR1402500).

■ REFERENCES

(1) Schlücker, S. *Angew. Chem., Int. Ed.* **2014**, *53*, 4756–4795.
(2) Nie, S.; Emory, S. R. *Science* **1997**, *275*, 1102–1106.
(3) Grubisha, D. S.; Lipert, R. J.; Park, H.-Y.; Driskell, J.; Porter, M. D. *Anal. Chem.* **2003**, *75*, 5936–5943.
(4) Ding, S.-Y.; Yi, J.; Li, J.-F.; Ren, B.; Wu, D.-Y.; Panneerselvam, R.; Tian, Z.-Q. *Nat. Rev. Mater.* **2016**, *1*, 16021.
(5) Li, J. F.; Huang, Y. F.; Ding, Y.; Yang, Z. L.; Li, S. B.; Zhou, X. S.; Fan, F. R.; Zhang, W.; Zhou, Z. Y.; Wu, D. Y.; Ren, B.; Wang, Z. L.; Tian, Z. Q. *Nature* **2010**, *464*, 392–395.
(6) Lombardi, J. R.; Birke, R. L. *J. Phys. Chem. C* **2014**, *118*, 11120–11130.
(7) Ling, X.; Huang, S.; Deng, S.; Mao, N.; Kong, J.; Dresselhaus, M. S.; Zhang, J. *Acc. Chem. Res.* **2015**, *48*, 1862–1870.
(8) Han, X. X.; Ji, W.; Zhao, B.; Ozaki, Y. *Nanoscale* **2017**, *9*, 4847–4861.
(9) Wang, X.; Shi, W.; Jin, Z.; Huang, W.; Lin, J.; Ma, G.; Li, S.; Guo, L. *Angew. Chem., Int. Ed.* **2017**, *56*, 9851–9855.
(10) Lin, J.; Shang, Y.; Li, X.; Yu, J.; Wang, X.; Guo, L. *Adv. Mater.* **2017**, *29*, 1604797.
(11) Yilmaz, M.; Babur, E.; Ozdemir, M.; Gieseking, R. L.; Dede, Y.; Tamer, U.; Schatz, G. C.; Facchetti, A.; Usta, H.; Demirel, G. *Nat. Mater.* **2017**, *16*, 918–924.
(12) Li, X.; Tao, L.; Chen, Z.; Fang, H.; Li, X.; Wang, X.; Xu, J.-B.; Zhu, H. *Appl. Phys. Rev.* **2017**, *4*, 021306.
(13) Tao, L.; Chen, Z.; Li, X.; Yan, K.; Xu, J.-B. *npj 2D Mater. Appl.* **2017**, *1*, 19.
(14) Wen, J.; Wang, H.; Wang, W.; Deng, Z.; Zhuang, C.; Zhang, Y.; Liu, F.; She, J.; Chen, J.; Chen, H.; Deng, S.; Xu, N. *Nano Lett.* **2017**, *17*, 4689–4697.
(15) Ling, X.; Xie, L.; Fang, Y.; Xu, H.; Zhang, H.; Kong, J.; Dresselhaus, M. S.; Zhang, J.; Liu, Z. *Nano Lett.* **2010**, *10*, 553–561.
(16) Ling, X.; Fang, W.; Lee, Y.-H.; Araujo, P. T.; Zhang, X.; Rodriguez-Nieva, J. F.; Lin, Y.; Zhang, J.; Kong, J.; Dresselhaus, M. S. *Nano Lett.* **2014**, *14*, 3033–3040.
(17) Feng, S.; dos Santos, M. C.; Carvalho, B. R.; Lv, R.; Li, Q.; Fujisawa, K.; Elias, A. L.; Lei, Y.; Perea-Lopez, N.; Endo, M.; Pan, M.; Pimenta, M. A.; Terrones, M. *Sci. Adv.* **2016**, *2*, e1600322.
(18) Yin, Y.; Miao, P.; Zhang, Y.; Han, J.; Zhang, X.; Gong, Y.; Gu, L.; Xu, C.; Yao, T.; Xu, P.; Wang, Y.; Song, B.; Jin, S. *Adv. Funct. Mater.* **2017**, *27*, 1606694.
(19) Zheng, Z.; Cong, S.; Gong, W.; Xuan, J.; Li, G.; Lu, W.; Geng, F.; Zhao, Z. *Nat. Commun.* **2017**, *8*, 1993.
(20) Peimyoo, N.; Li, J.; Shang, J.; Shen, X.; Qiu, C.; Xie, L.; Huang, W.; Yu, T. *ACS Nano* **2012**, *6*, 8878–8886.
(21) Lin, J.; Liang, L.; Ling, X.; Zhang, S.; Mao, N.; Zhang, N.; Sumpter, B. G.; Meunier, V.; Tong, L.; Zhang, J. *J. Am. Chem. Soc.* **2015**, *137*, 15511–15517.
(22) Cong, S.; Yuan, Y.; Chen, Z.; Hou, J.; Yang, M.; Su, Y.; Zhang, Y.; Li, L.; Li, Q.; Geng, F.; Zhao, Z. *Nat. Commun.* **2015**, *6*, 7800.
(23) Zheng, X.; Ren, F.; Zhang, S.; Zhang, X.; Wu, H.; Zhang, X.; Xing, Z.; Qin, W.; Liu, Y.; Jiang, C. *ACS Appl. Mater. Interfaces* **2017**, *9*, 14534–14544.
(24) Soluyanov, A. A.; Gresch, D.; Wang, Z.; Wu, Q.; Troyer, M.; Dai, X.; Bernevig, B. A. *Nature* **2015**, *527*, 495–498.
(25) Qian, X.; Liu, J.; Fu, L.; Li, J. *Science* **2014**, *346*, 1344–1347.
(26) Ali, M. N.; Xiong, J.; Flynn, S.; Tao, J.; Gibson, Q. D.; Schoop, L. M.; Liang, T.; Haldolaarachchige, N.; Hirschberger, M.; Ong, N. P.; Cava, R. J. *Nature* **2014**, *514*, 205–208.
(27) Zhou, J.; Liu, F.; Lin, J.; Huang, X.; Xia, J.; Zhang, B.; Zeng, Q.; Wang, H.; Zhu, C.; Niu, L.; et al. *Adv. Mater.* **2017**, *29*, 1603471.
(28) Chen, K.; Chen, Z.; Wan, X.; Zheng, Z.; Xie, F.; Chen, W.; Gui, X.; Chen, H.; Xie, W.; Xu, J. *Adv. Mater.* **2017**, *29*, 1700704.

DOI: 10.1021/jacs.8b02972
J. Am. Chem. Soc. 2018, 140, 8696–8704

(29) Kim, Y.; Jhon, Y. I.; Park, J.; Kim, J. H.; Lee, S.; Jhon, Y. M. *Nanoscale* **2016**, *8*, 2309−2316.
(30) Qi, Y.; Naumov, P. G.; Ali, M. N.; Rajamathi, C. R.; Schnelle, W.; Barkalov, O.; Hanfland, M.; Wu, S.-C.; Shekhar, C.; Sun, Y.; et al. *Nat. Commun.* **2016**, *7*, 11038.
(31) Voiry, D.; Mohite, A.; Chhowalla, M. *Chem. Soc. Rev.* **2015**, *44*, 2702−2712.
(32) Xie, L.; Ling, X.; Fang, Y.; Zhang, J.; Liu, Z. *J. Am. Chem. Soc.* **2009**, *131*, 9890−9891.
(33) Tao, L.; Chen, K.; Chen, Z.; Chen, W.; Gui, X.; Chen, H.; Li, X.; Xu, J.-B. *ACS Appl. Mater. Interfaces* **2017**, *9*, 12073−12081.
(34) Tao, L.; Qiu, C.; Yu, F.; Yang, H.; Chen, M.; Wang, G.; Sun, L. *J. Phys. Chem. C* **2013**, *117*, 10079−10085.
(35) Lee, Y.; Kim, H.; Lee, J.; Yu, S. H.; Hwang, E.; Lee, C.; Ahn, J.-H.; Cho, J. H. *Chem. Mater.* **2016**, *28*, 180−187.
(36) Lukowski, M. A.; Daniel, A. S.; Meng, F.; Forticaux, A.; Li, L.; Jin, S. *J. Am. Chem. Soc.* **2013**, *135*, 10274−10277.
(37) Ling, X.; Wu, J.; Xie, L.; Zhang, J. *J. Phys. Chem. C* **2013**, *117*, 2369−2376.
(38) Qiu, C.; Zhou, H.; Yang, H.; Chen, M.; Guo, Y.; Sun, L. *J. Phys. Chem. C* **2011**, *115*, 10019−10025.
(39) Song, J.; Huang, Y.; Fan, Y.; Zhao, Z.; Yu, W.; Rasco, B.; Lai, K. *Nanomaterials* **2016**, *6*, 175.
(40) Xie, W.; Walkenfort, B.; Schlücker, S. *J. Am. Chem. Soc.* **2013**, *135*, 1657−1660.
(41) Xu, W.; Ling, X.; Xiao, J.; Dresselhaus, M. S.; Kong, J.; Xu, H.; Liu, Z.; Zhang, J. *Proc. Natl. Acad. Sci. U. S. A.* **2012**, *109*, 9281−9286.
(42) Kang, Z.; Chen, J.; Ho, H.-P. *Nanoscale* **2016**, *8*, 10266−10272.
(43) Zhao, Y.; Xie, Y.; Bao, Z.; Tsang, Y. H.; Xie, L.; Chai, Y. *J. Phys. Chem. C* **2014**, *118*, 11827−11832.
(44) Muehlethaler, C.; Considine, C. R.; Menon, V.; Lin, W.-C.; Lee, Y.-H.; Lombardi, J. R. *ACS Photonics* **2016**, *3*, 1164−1169.
(45) Liu, H.; Han, N.; Zhao, J. *RSC Adv.* **2015**, *5*, 17572−17581.
(46) Lombardi, J. R.; Birke, R. L. *J. Phys. Chem. C* **2008**, *112*, 5605−5617.
(47) Shegai, T.; Vaskevich, A.; Rubinstein, I.; Haran, G. *J. Am. Chem. Soc.* **2009**, *131*, 14390−14398.
(48) Lombardi, J. R.; Birke, R. L.; Lu, T.; Xu, J. *J. Chem. Phys.* **1986**, *84*, 4174−4180.
(49) Jensen, L.; Schatz, G. C. *J. Phys. Chem. A* **2006**, *110*, 5973−5977.
(50) Morton, S. M.; Jensen, L. *J. Am. Chem. Soc.* **2009**, *131*, 4090−4098.
(51) Fainstein, A.; Jusserand, B. *Phys. Rev. B: Condens. Matter Mater. Phys.* **1998**, *57*, 2402−2406.

DOI: 10.1021/jacs.8b02972
J. Am. Chem. Soc. 2018, 140, 8696−8704